

Equation of state and optical properties of warm dense helium

P. M. Kowalski,^{1,2,3} S. Mazevet,⁴ D. Saumon,² and M. Challacombe⁵

¹*Department of Physics and Astronomy, Vanderbilt University, Nashville, Tennessee 37235, USA*

²*Applied Physics Division, Los Alamos National Laboratory, Los Alamos, New Mexico 87545, USA*

³*Lehrstuhl für Theoretische Chemie, Ruhr-Universität Bochum, D-44780 Bochum, Germany*

⁴*Département de Physique Théorique et Appliquée, CEA, Boîte Postale 12 91680 Bruyères le Châtel, France*

⁵*Theoretical Division, Los Alamos National Laboratory, Los Alamos, New Mexico 87545, USA*

(Received 27 February 2007; revised manuscript received 14 June 2007; published 10 August 2007)

We investigate the physical properties of warm dense helium under the conditions found in the atmospheres of cool white dwarfs using both a chemical model and *ab initio* simulations. A chemical model is developed for the low-ionization limit that includes the species He, He⁺, He₂⁺, and electrons, and interactions between them. The *ab initio* calculations consist in quantum molecular dynamics (QMD) simulations. We use the generalized gradient approximation (GGA) to calculate the equation of state and the electrical and optical properties within the linear response theory. We further use an exact exchange hybrid (PBE0) density functional as well as the GW approximation to estimate the uncertainties on the electrical and optical properties resulting from the GGA approximation. While both the chemical model and the QMD simulations are in excellent agreement with the measured equation of state, a qualitative discrepancy exists with the measured conductivity.

DOI: [10.1103/PhysRevB.76.075112](https://doi.org/10.1103/PhysRevB.76.075112)

PACS number(s): 72.20.-i, 71.15.Pd, 71.15.Mb, 64.30.+t

I. INTRODUCTION

White dwarf stars are the end stage of the evolution of most stars. Having exhausted their nuclear fuel, they cool simply by radiating their heat content to space at a rate that, in the coolest white dwarfs, is controlled by the opacity of the atmosphere (the semitransparent surface layer where radiation escapes to space).¹ In general, cool white dwarf atmospheres are composed of hydrogen, helium, or a mixture thereof. Modeling these atmospheres requires a knowledge of the physical properties of He and H-He mixtures at high densities (a few g/cm³) and low temperatures ($T \lesssim 10^4$ K) where conventional methods to calculate the opacity, which are suitable for the ideal gas, usually fail.² The equation of state of helium in this regime is also of interest for modeling the interiors of Jupiter, Saturn, and gaseous extrasolar planets.^{3,4}

Despite its astrophysical importance, warm dense helium has received relatively little attention from experimentalists and theorists alike. Experimental data are limited to a few shock compression equation of state (EOS) points below 60 GPa (Ref. 5) and conductivities up to ~ 160 GPa.⁶ Reflectivity measurements under shock compression are under way.⁷ A few large EOS tables that model the regime of pressure ionization have been computed with chemical models⁸⁻¹⁰ but they are poorly constrained in the regime of interest as demonstrated by the wide range of predictions for the density at which helium pressure ionizes (from ~ 0.3 to 10 g/cm³). These EOS models aim at a description of helium over a very broad range of physical conditions and are not suitable for estimating the degree of ionization in the regime of weak pressure ionization. Recent *ab initio* simulations of fluid helium have focused on the maximum compression along the principal Hugoniot¹¹ and the nonmetal-metal transition.¹²

In this paper, we model the EOS and the electrical and optical properties of pure helium under the conditions found

in cool white dwarf atmospheres, where $\rho \lesssim 2$ g/cm³ and $T \lesssim 1$ eV. Under these conditions, the challenge is to calculate the free-free absorption due to a very small but nonetheless crucial fraction of free electrons in a dense fluid. To address this problem, we have performed a suite of *ab initio* simulations and developed a detailed model within the chemical picture. Calculations were also performed at temperatures and densities above these values for comparison with experimental data and to explore more completely the properties of helium.

The chemical model assumes the existence of the chemical species: He, He⁺, He₂⁺, and *e*, whose abundances in the low-ionization limit ($T \lesssim 1$ eV) are determined by minimizing the free energy of the system. We improve the treatment of interactions between He atoms and trace species, especially the strong He-*e* interaction. The conductivity is estimated from the density of free electrons and a simple conductivity model. The great advantage of the chemical model is its computational expediency. It is more readily generalized to H-He mixtures and it is easily implemented in applications. It also recovers the dilute gas limit which is not accessible to simulations but is required for modeling stellar atmospheres. Finally, it can be modified to better reproduce the experimental data or other calculations.

We performed fixed-temperature quantum molecular dynamics (QMD) simulations where the electrons receive a full quantum mechanical treatment using finite temperature density functional theory (DFT),¹³ while the classical ions are propagated in time using the force field resulting from the calculated electronic charge density and the ionic configuration of the system. We obtain the optical properties of dense helium by first calculating the electrical conductivity within the linear response theory and using the Kubo-Greenwood formulation.^{14,15} We further establish the uncertainties on the electrical and optical properties resulting from the underestimation of the band gap by ground state DFT methods by performing calculations using a hybrid functional and GW calculations.¹⁶

We compare the results from both models with measurements of the EOS and conductivity of shock compressed helium. We find that both models are in good agreement with the EOS shock data.⁵ In contrast, the conductivity measured at densities of about 1 g cm^{-3} and at temperatures of $1\text{--}2.35 \text{ eV}$ (Ref. 6) as well as its temperature and density behavior cannot be reproduced by quantum molecular dynamics simulations. By calculating band gap corrections using a hybrid functional and the GW method, we further show that the shortcoming of the DFT method cannot be the source of this discrepancy. We finally compare the absorption and the index of refraction obtained with the *ab initio* calculations with a model developed for white dwarf atmospheres² and find large differences in both shape and magnitude in the relevant range of photon energies ($<10 \text{ eV}$).

II. CHEMICAL MODEL

A. Description

Motivated by the conditions found in the atmospheres of cool white dwarfs, we developed a chemical model for the ionization of He in the limit of very low ionization fraction ($\leq 1\%$). This condition is satisfied for $T \leq 1.5 \text{ eV}$ and $\rho \leq 1.6 \text{ g cm}^{-3}$. The chemical model includes the contributions from the species He, He^+ , He_2^+ , and e to the Helmholtz free energy of the system. Doubly ionized helium (He^{2+}) is also included but its contribution is extremely small in the regime of interest and will not be discussed further. The free energy is written as

$$F = F_{\text{kin}} + F_{\text{int}} + F_{\text{conf}}, \quad (1)$$

where

$$F_{\text{kin}} = \sum_i N_i kT \left\{ \ln \left[\frac{N_i}{V} \left(\frac{2\pi\hbar^2}{m_i kT} \right)^{3/2} \right] - 1 \right\} \quad (2)$$

is the contribution from the kinetic degrees of freedom (Maxwell-Boltzmann) from all species (including electrons), and

$$F_{\text{int}} = -kT \sum_i N_i \ln Z_i + N_i I_i \quad (3)$$

is the contribution from the internal degrees of freedom of He, He^+ , and He_2^+ , where Z_i is the internal partition function

$$Z_i = \sum_k g_k e^{-\beta \epsilon_{ik}}. \quad (4)$$

Finally,

$$F_{\text{conf}} = F_{\text{conf}}(\text{He-He}) + F_{\text{conf}}(\text{He-He}^+) + F_{\text{conf}}(\text{He-He}_2^+) + F_{\text{conf}}(\text{He-e}) \quad (5)$$

accounts for the interactions of each species with the dominant atomic He. Because we restrict the model to very low ionization, electron degeneracy (Fermi-Dirac statistics) and Coulomb interactions between charged particles are negligible. In the above expressions, $\beta = 1/kT$, N_i is the number of particles of species i , V is the volume of the system, m_i is the

mass of the particle, ϵ_{ik} is the energy of bound state k of species i , measured with respect to the ground state, I_i is the energy of the ground state of species i with respect to the ground state of the He atom, and the other symbols have their usual meaning.

Due to the very high first level energies of isolated He and He^+ compared to our temperature range of $T \leq 1.5 \text{ eV}$, their internal partition functions are very well approximated by their ground state contributions only. For He_2^+ , we use the partition function of Stancil.¹⁷ The energy of the ground state of each species relative to that of He is $I_1 = 24.5874 \text{ eV}$ for He^+ and $I_2 = 22.222 \text{ eV}$ for He_2^+ .¹⁸

For a given T and ρ , the chemical equilibrium abundances are obtained by minimizing the total free energy with respect to the particle number for each species, N_i , and subject to the constraints of charge neutrality,

$$N(e) = N(\text{He}^+) + N(\text{He}_2^+), \quad (6)$$

and mass conservation,

$$\rho = \frac{1}{V} \sum_i N_i m_i. \quad (7)$$

For our system of four species, the chemistry can be written as



Minimizing the free energy for fixed T and V , the chemical equilibrium is obtained when

$$\mu(\text{He}) = \mu(\text{He}^+) + \mu(e), \quad (10)$$

$$\mu(\text{He}_2^+) = \mu(\text{He}) + \mu(\text{He}^+), \quad (11)$$

where

$$\mu_i = \left. \frac{\partial F}{\partial N_i} \right|_{V, T, \{N_{j \neq i}\}} \quad (12)$$

is the chemical potential of species i , a sum of kinetic, internal, and configuration (excess) terms. Using explicit expressions for the μ_i , Eqs. (10) and (11) lead to

$$\begin{aligned} \frac{n(\text{He})}{n(\text{He}^+)n(e)} &= \frac{Z_{\text{He}}}{2Z_{\text{He}^+}} \left(\frac{2\pi\hbar^2}{kT} \right)^{3/2} \left(\frac{m_{\text{He}}}{m_e m_{\text{He}^+}} \right)^{3/2} \\ &\times \exp\{\beta[I_1 - \mu_{\text{conf}}(\text{He}) + \mu_{\text{conf}}(\text{He}^+) \\ &+ \mu_{\text{conf}}(e)]\} \end{aligned} \quad (13)$$

and

$$\begin{aligned} \frac{n(\text{He}_2^+)}{n(\text{He}^+)n(\text{He})} &= \frac{Z_{\text{He}_2^+}}{Z_{\text{He}^+}Z_{\text{He}}} \left(\frac{2\pi\hbar^2}{kT} \right)^{3/2} \left(\frac{m_{\text{He}_2^+}}{m_{\text{He}}m_{\text{He}^+}} \right)^{3/2} \\ &\times \exp\{\beta[I_1 - I_2 - \mu_{\text{conf}}(\text{He}_2^+) + \mu_{\text{conf}}(\text{He}^+) \\ &+ \mu_{\text{conf}}(\text{He})]\}, \end{aligned} \quad (14)$$

respectively, where $n(i) = N_i/V$ is the number density and $\mu_{\text{conf}}(i)$ is the excess chemical potential.

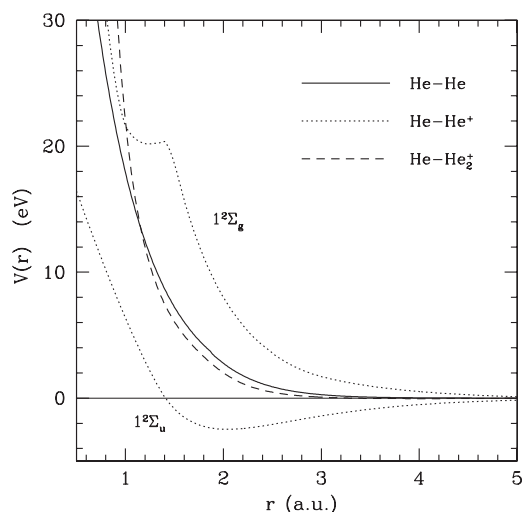


FIG. 1. Pair potentials used in the chemical model. For the He-He⁺ potential, both the bonding ($1^2\Sigma_u$) and the antibonding ($1^2\Sigma_g$) states are shown.

In the limit of low ionization, $\mu_{\text{conf}}(i)$ depends only on $n(\text{He})$ and T and can be tabulated prior to the calculation of the chemical equilibrium. For given pair interaction potentials between species i and He, the pair correlation function, the excess chemical potential, and other excess thermodynamic quantities are obtained by solving the Ornstein-Zernike equation in the Percus-Yevick approximation.

B. Interaction potentials

The He-He interactions, which dominate the thermodynamics of the chemical model, are described by an effective pair potential calibrated to single- and double-shock data and the melting curve of helium.¹⁹ The He-He₂⁺ pair potential is based on *ab initio* quantum mechanical calculations²⁰ and a spherical average of its angular dependence is performed prior to calculating $\mu_{\text{conf}}(\text{He}_2^+)$. The pair potentials are shown in Fig. 1. The remaining two interaction potentials that enter the chemical model require more attention and are described below.

1. He-He⁺ interaction potential

Quantum mechanical calculations of the He-He⁺ dimer show that there are two interaction curves that lead to ground state He and He⁺ at large separations, the $1^2\Sigma_u$ state (bonding) and the $1^2\Sigma_g$ state (antibonding). Both potentials have a multiplicity of 2. Scattering experiments^{21,22} show that averaging the two potentials is representative of the interaction only for $T > 1$ keV, well above the regime of interest. At lower temperatures, both potentials must be considered for the He-He⁺ interaction.²¹ We have therefore modeled the interaction of a He⁺ ion surrounded by He atoms by considering that 1/2 of the He atoms will interact with the $1^2\Sigma_u$ potential curve and 1/2 with the $1^2\Sigma_g$ potential curve (Fig. 1).

The He-He⁺ interaction potential should be corrected at high densities for many-body effects. The relatively deep

well of the He-He⁺ $1^2\Sigma_u$ potential (Fig. 1) leads to the formation of a covalent bond where electrons are shared between the two He nuclei. At high density, we can expect sharing of electrons between multiple nuclei (delocalization of the binding electrons) and N -body corrections to be larger than for the other potentials. Unfortunately, there are no experimental data or calculations to estimate the weakening of the well of the He-He⁺ potential at high densities and the only choice at present is to use the *ab initio* potentials for isolated pairs.

2. He-electron excess energy

It is common practice in chemical models to describe the interaction between electrons and atoms with a polarization potential²³ which is attractive at long range. A hard cutoff may be introduced to provide short range repulsion.^{10,24,25} While the polarization potential is adequate at low densities and large separation, low-energy scattering experiments²⁶ show that the effective local He- e potential, while repulsive at short range, is more complex than a simple repulsive wall. Furthermore, in the low-temperature, high-density regime of interest, the electron interactions cannot be treated classically because its thermal wavelength overlaps several He atoms. In view of these difficulties, we have opted for computing the interaction energy of an electron in a dense helium bath with density functional theory. We compute the energy difference between two ground state calculations of a simulation box that contains $2N+1$ electrons and one that contains $2N$ electrons, where N is the number of helium nuclei in the box in a fixed configuration.

For this purpose, we generated classical Monte Carlo²⁷ configurations of $N=32$ He atoms in the canonical ensemble with the effective He-He pair potential mentioned above.¹⁹ For a fixed configuration of ions, the electronic ground state energy $E_e(2N)$ of the $2N$ electrons is solved using DFT and periodic boundary conditions. The energy of a free electron in a bath of helium is then given by $E_e = E_e(2N+1) - E_e(2N)$. We take the average of E_e from nine ionic configurations at each temperature and density point. We have verified that simulations using $N=32$ ions give a converged value of E_e to within ~ 0.1 eV by running simulations up to $N=256$ (Fig. 2). The E_e calculations were performed using the ABINIT code^{28,29} and using both the local density approximation (LDA)³⁰ and a generalized gradient approximation (GGA) [Perdew-Burke-Ernzerhof³¹ (PBE)] density functional. We also calculated E_e using the ESPRESSO code³² with the Becke-Lee-Yang-Parr (BLYP) GGA functional.^{33,34} The calculations were performed for densities between 0.5 and 4 g/cm³ and $T=0-1$ eV. The calculations show that E_e is a linear function of the density of He atoms (Fig. 3). Linear least squares fits to the three calculations show that they have the same slope within the statistical uncertainties of the simulations. The BLYP functional is known to give better results for electron affinities³⁵ and our calculation with the BLYP functional is the most consistent with the experimental data³⁶ (obtained at $\rho < 0.2$ g cm⁻³ and $T < 100$ K). For these reasons, we use the BLYP calculation as our best estimate of the energy of an electron in dense fluid He.

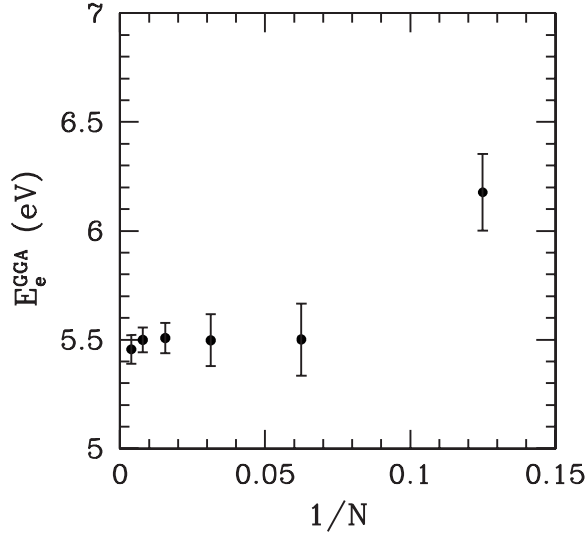


FIG. 2. Convergence of the electron energy E_e in dense helium as a function of the number of He atoms N in the simulation. The calculation shown is for $T=0.5$ eV and $\rho=1$ g cm $^{-3}$.

Finally, we have performed a few full MD-DFT test simulations to allow the ion configuration to relax with the $2N+1$ electron wave function. The resulting E_e agree with the ABINIT-PBE (GGA) calculation to within 0.2 eV. This also shows that the presence of the additional electron does not affect the configuration of the atoms in this regime, and therefore the excess entropy of the free electron is small compared to the interaction energy. This is consistent with the interpretation of measurements of the electron mobility in cryogenic helium, where the electron does not form a cavity by repulsion of the He atoms.³⁷

The BLYP calculation of $E_e(T, n(\text{He}))$ has been fitted with a linear functional form for $n(\text{He}) > 0.05$ g/cm 3 . At low den-

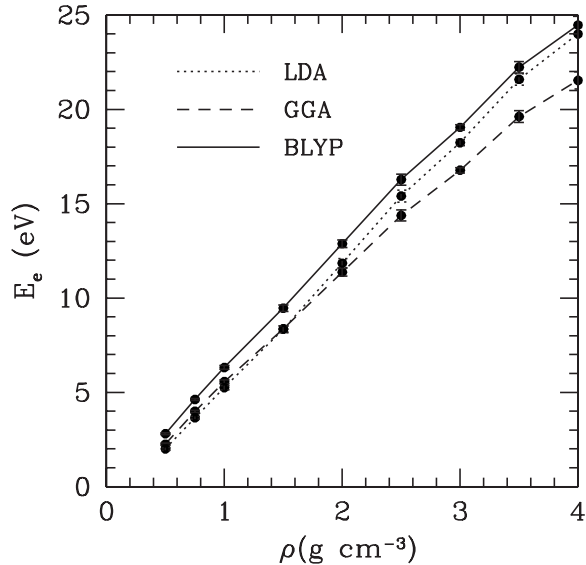


FIG. 3. Energy of an electron in dense helium based on DFT calculations. Each curve corresponds to a different calculation: ESPRESSO (BLYP), ABINIT (GGA-PBE), and ABINIT (LDA). All three curves are for $T=0.5$ eV.

TABLE I. Table of coefficients for the electron affinity [Eqs. (14)–(18)].

| | |
|----------|------------------------------|
| ρ_0 | 0.05 g cm $^{-3}$ |
| a_1 | 8.60384 eV cm 3 g $^{-1}$ |
| a_2 | -4.83886 eV $^{-1}$ |
| a_3 | 1.97586 eV $^{-2}$ |
| b_0 | 1.0313 |
| b_1 | 2.99678 eV $^{-1}$ |
| b_2 | 10.3747 eV $^{-2}$ |
| b_3 | 2.99498 eV $^{-3}$ |
| b_4 | -1.27844 eV $^{-4}$ |
| b_5 | -3.10191 eV $^{-5}$ |

sities, the energy of an electron in helium is given by the Lenz formula^{36,38}

$$E_{el}^{\text{Lenz}} = \frac{2\pi\hbar^2 n(\text{He}) a_{\text{He}}(T)}{m_e} = C_L(T)\rho, \quad (15)$$

where $a_{\text{He}}(T) \sim 0.6-0.7$ Å is the electron-He scattering length³⁹ that reproduces the experiments⁴⁰ for $T < 1$ eV. The Lenz formula is also linear in $n(\text{He})$ and reproduces experimental data at low densities.^{36,38} Corrections to the Lenz formula are expected for moderate densities of ~ 0.05 g cm $^{-3}$,³⁶ so we use a quadratic form that recovers the Lenz formula at very low density and smoothly joins the fit of the DFT-BLYP calculation of $E_e(T, n(\text{He}))$. The final result is

$$E_e(\rho, T) = 10[\alpha(T) - C_L]\rho^2 + C_L\rho, \quad (16)$$

for $\rho < \rho_0$ and

$$E_e(\rho, T) = \alpha(T)\rho + 10[\alpha(T) - C_L]\rho_0^2 + [C_L - \alpha(T)]\rho_0, \quad (17)$$

for $\rho \geq \rho_0$, where

$$\alpha(T) = a_1 e^{a_2 T + a_3 T^2} \sum_{i=0.5} b_i T^i. \quad (18)$$

E_e and T are in eV, ρ is in g cm $^{-3}$, and the coefficients are given in Table I.

Isotherms of E_e are shown in Fig. 4. The agreement with the low-temperature data³⁶ is excellent and the T dependence is weak. We find that E_e is always positive and becomes large for $\rho \geq 0.1$ g/cm 3 , which is consistent with independent calculations.⁴¹ The He- e interaction thus tends to inhibit the pressure ionization of He.

Since the entropy contribution associated with the He- e interaction (excluded volume interaction) is small compared to E_e ($E_e \gg TS_e$), $\mu_{\text{conf}}(e) = \partial F_e / \partial N_e \approx E_e$, where F_e is the excess Helmholtz free energy and $\mu_{\text{conf}}(e)$ is the configuration chemical potential.

III. QUANTUM MOLECULAR DYNAMICS SIMULATIONS

For the quantum molecular simulations presented here, we used the VASP *ab initio* simulation code.⁴² The simula-

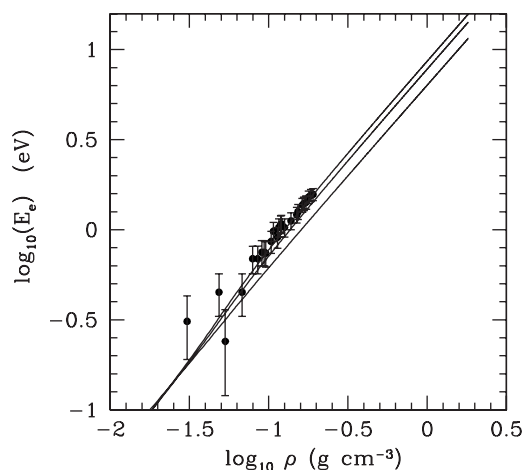


FIG. 4. Energy of an electron in helium as a function of density [Eqs. (16) and (17)]. Each curve corresponds to an isotherm with $T=10$, 5000, and 10^4 K (from top to bottom). The experimental data were taken in the 10–100 K range (Ref. 36).

tions were ran for typically 2 ps with time steps ranging from 2 fs for the lowest densities to 0.5 fs at the highest, and using 54 and 128 atoms in the simulation cell. We used a projected augmented wave (PAW) pseudopotential in the Perdew-Wang 91 (PW91)⁴³ parametrization of the GGA.⁴⁴ We paid particular attention to the convergence of the various properties of interest as a function of the plane wave energy cutoff. This issue was recently raised for the case of hydrogen.⁴⁵ For helium, we find that it is necessary to use a cutoff energy of 800 eV to converge in pressure. In contrast to the hydrogen findings, we find that the real space projection used in the QMD calculations does not introduce significant error for the pressure or the internal energy.

IV. EQUATION OF STATE

A. Results from QMD

In Fig. 5, we compare the QMD Hugoniot with the experimental data.⁵ The Rankine-Hugoniot equation⁴⁶

$$(U_0 - U_1) + \frac{1}{2}(V_0 - V_1)(P_0 + P_1) = 0 \quad (19)$$

describes the shocked state through a relation between the initial and final volumes, internal energy, and pressure, respectively, (V_0, U_0, P_0) and (V_1, U_1, P_1) . For a given V_1 , a least squares fit of the MD-DFT values of P_1 and U_1 with a quadratic function in T is used to solve Eq. (19).⁴⁷

For the principal Hugoniot calculation, the initial condition used is $P_0=0$ GPa, and $\rho_0=0.1245$ g/cm³, in agreement with the experimental data. The reference energy point for the QMD calculations is defined as $U_0=0$ eV/atom, obtained after subtracting from the QMD internal energies the computed internal energy of an isolated atom in a box of 12 Å on a side. For the principal Hugoniot, the agreement at the highest pressure measured is excellent. For the reshocked points, we used the QMD Hugoniot point obtained at the highest pressure as an initial condition: $\rho_1=0.4$ g/cm³, $U_1=1.7$ eV/atom and $P_1=14.7$ GPa. The highest QMD re-

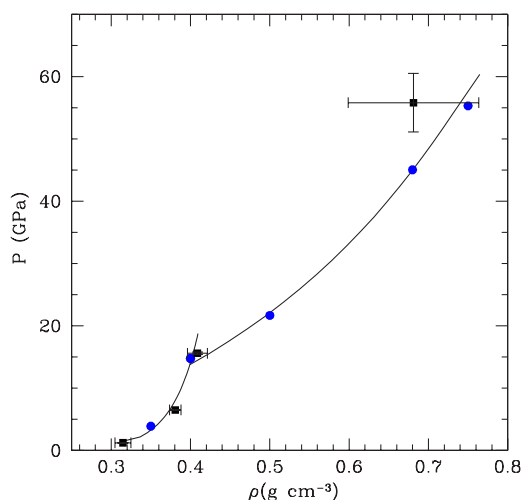


FIG. 5. (Color online) Principal and second-shock Hugoniot of helium as a function of density. The experimental data (Ref. 5) are shown by squares with error bars. Solid dots (blue) show the QMD calculation and the two solid curves represent the first- and second-shock Hugoniot computed with the chemical model. The latter also guide the eye through the experimental and QMD first- and second-shock points.

shocked point calculated also agrees with the experimental measurement within the error bars. While the high pressure experimental data are very sparse, it is reassuring to find that the QMD calculations agree very well with the data as these four experimental points are used extensively to adjust the helium EOS at high pressures. The QMD calculations indicate, however, a slightly softer reshock Hugoniot, in agreement with the EOS obtained using the chemical model (Sec. IV B) and independent *ab initio* simulations.^{11,12}

B. Results from the chemical model

With the configuration contribution to the chemical potentials $\mu_{\text{conf}}(i)$ derived above, the chemical equilibrium abundances of each species are obtained by solving Eqs. (6), (7), (10), and (11) and all the thermodynamics quantities of interest follow directly. The composition of this interacting helium fluid model is shown in Fig. 6 for two temperatures. The mole fraction of He_2^+ remains below 10^{-6} for $T < 1$ eV so this ion plays a minor role in the ionization balance of helium which is dominated by He^+ . The configuration contributions, which are responsible for pressure ionization, become noticeable for $\rho \gtrsim 0.3$ g/cm³. The ionization fraction rises rapidly at higher densities but remains below 0.1% even up to $\rho = 1.5$ g/cm³. This low-ionization model for helium is valid for $\rho \leq 1.6$ g/cm³ and $T \leq 1.5$ eV. At higher temperatures or densities, the Coulomb interactions between e and He^+ that we have neglected become important. At higher densities still, electron degeneracy is no longer negligible.

On the other hand, the thermodynamics of the chemical model is in excellent agreement with the MD-DFT simulations up to $\rho = 2$ g/cm³. The first- and second-shock Hugoniot also agree very well with the experimental data (Fig. 5), as well as with the MD-DFT simulations. This is not

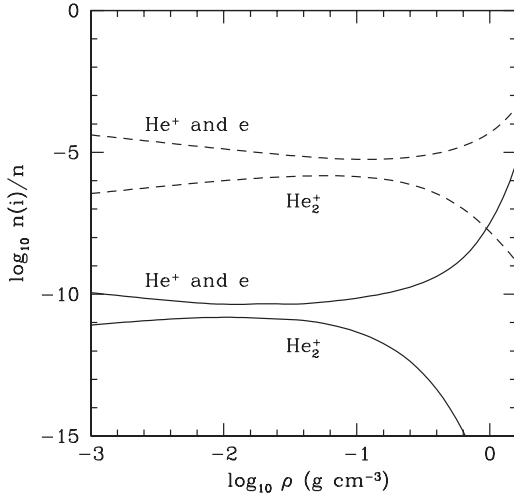


FIG. 6. Chemical equilibrium in the He chemical model. The mole fractions $n(i)/n$, where $n = \sum_i n(i)$, are shown as a function of density for $T=0.5$ eV (solid curves) and $T=1$ eV (dashed curves). Since the electron mole fraction is given by $n(e) = n(\text{He}^+) + n(\text{He}_2^+)$ and $n(\text{He}_2^+) \ll n(\text{He}^+)$, the electron mole fraction is indistinguishable from that of He^+ .

surprising since, as mentioned above, the effective He-He pair potential was adjusted to reproduce the shock data.⁵ In the limit of low ionization for which this model was developed, the thermodynamics is indeed dominated by the contribution from atomic He.

V. BAND GAP AND ELECTRICAL PROPERTIES

We now turn to the principal motivation of the current study which is the calculation of the electrical and optical properties of helium at high pressures and for conditions relevant to white dwarf atmospheres. From the QMD trajectories produced, we calculate the electrical properties on a set of configurations using the Kubo-Greenwood formulation of the optical conductivity where the real part is given as^{14,15}

$$\text{Re } \sigma(\omega) = \frac{2\pi e^2}{3\omega} \frac{1}{\Omega} \sum_{\mathbf{k}} W(\mathbf{k}) \sum_{n,m} (f_n^{\mathbf{k}} - f_m^{\mathbf{k}}) |\langle \psi_n^{\mathbf{k}} | \vec{\nabla} | \psi_m^{\mathbf{k}} \rangle|^2 \delta(E_m^{\mathbf{k}} - E_n^{\mathbf{k}} - \hbar\omega). \quad (20)$$

In Eq. (20), ω is the frequency, e is the electron charge, $\psi_n^{\mathbf{k}}$ and $E_n^{\mathbf{k}}$ are the electronic eigenfunctions and eigenvalues for the electronic band n at a given \mathbf{k} point in the Brillouin zone, $W(\mathbf{k})$ is the \mathbf{k} -point weight in the Brillouin zone using the Monkhorst-Pack scheme,⁴⁸ and $f_n^{\mathbf{k}}$ is the Fermi distribution function. $\vec{\nabla}$ is the velocity operator and Ω the volume of the simulation cell. Finally, the Kubo-Greenwood formulation is applied using the all-electron PAW potential, which does not require the correction term related to the nonlocality of the pseudopotential that would be needed if, for example, an ultrasoft pseudopotential was used. Calculations were performed at the Γ point. Additional details on this type of calculation can be found in Ref. 49.

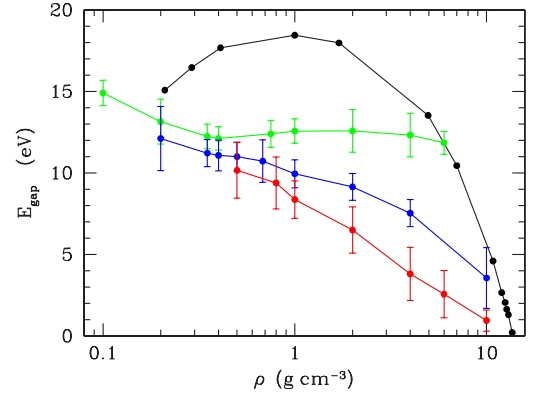


FIG. 7. (Color online) GGA band gap as a function of density for (from top to bottom) the $T=0$ fcc solid (black), and fluid QMD simulations at temperature $T_i=T_e=0.52$ eV (green), 1.5 eV (blue), and 3 eV (red), where T_i and T_e are the ion and electron temperatures, respectively. The error bars are calculated from the average obtained over the whole simulation.

A. GGA band gap

At normal conditions, helium in the ground state is an insulator with a rather large gap (~ 20 eV), which is defined as the energy difference between the highest occupied molecular orbital and the lowest unoccupied molecular orbital (HOMO-LUMO) at $T=0$. As can be seen from Eq. (20), the conductivity increases as the occupation of the conduction band (and hence, the ionization fraction) becomes large. This occurs when either the band gap diminishes or the temperature increases, or both. Figure 7 shows the variation of the Kohn-Sham (KS) band gap as a function of density and temperature as obtained using DFT (GGA functional). For a regular fcc lattice at $T=0$, the method predicts that the He band gap closes at a density of 13.5 g cm^{-3} in agreement with previous linear muffin-tin orbital calculations.⁵⁰ At finite temperature, the KS band gap that enters Eq. (20) is obtained by averaging the energy difference of the eigenstates on either side of the Fermi energy along the whole trajectory (Fig. 7). This definition of the gap recovers the HOMO-LUMO gap at $T=0$. The error bars are directly obtained from the fluctuations of the band gap along the trajectory. At low temperatures [0.5 eV (Ref. 51)], the KS band gap obtained from the simulations is almost constant in the density range investigated here. At higher temperatures, the band gap diminishes as a function of both density and temperature with a closure of the band gap predicted at around 10 g/cm^3 . The band gap of fluid helium is smaller than for the solid fcc structure as a result of increased disorder.

At low densities, the gap tends to a value of about 15 eV. For the isolated atom, calculation of the first excited state gives a value of 15.8 eV using either the PW91⁴³ or PBE³¹ functionals. The experimental value for the energy of the first excited state of He is 19.82 eV above the ground state. It is well known that the DFT method, which is a ground state approach and formally not suited for handling excited states, systematically underestimates band gaps.⁵² This deficiency of DFT methods is related to the discontinuity in the exchange-correlation potential when one electron is added to

the system,^{52–54} and it occurs even if the exact functional is used.⁵⁵ For open shell atoms, this discontinuity causes the eigenvalue of the highest occupied KS level to approximate the average of the ionization energy (I_p) and of the electron affinity (E_A)^{53,54} rather than the ionization energy. Usually, $I_p \gg E_A$ for atoms, leading to a significant underestimation of I_p and of the HOMO-LUMO band gap. The excited state energies E_m^k used in Eq. (20) are generally underestimated for semiconductors,^{52,56} which, in turn, leads to significant uncertainties in the calculation of the optical response.

The situation at finite temperature is not as clear and a systematic quantification of the uncertainties resulting from the use of ground state DFT for systems subject to temperatures in the eV range has yet to be conducted. A recent calculation suggests that this approximation may not be as drastic at finite temperature.⁵⁷ To quantify the uncertainties for the case of helium, we conducted calculations using hybrid functionals and the GW approximation. We performed these calculations at $T=0$ eV with the understanding that they provide an upper bound correction to the corresponding finite temperature results.

B. Hybrid functional (PBE0)

To investigate the band gap correction, we first performed DFT calculations using an exact exchange hybrid functional, PBE0,⁵⁸ with the chemistry code MONDOSCF, a program suite for $O(N)$ SCF theory and *ab initio* MD.⁵⁹ The PBE0 hybrid functional combines the orbital-dependent Hartree-Fock exchange and an explicit density functional, in the present case the GGA PBE functional.^{31,60} Among other properties, exact exchange functionals lead to improved calculations of the band gap at an accuracy comparable to that of GW calculations.^{16,61}

The MONDOSCF electronic structure code uses Gaussian basis sets. In extended systems, care must be taken when the density is varied as numerical linear dependences between the Gaussian basis functions arise when the basis contains orbitals that are too diffuse. We find that the situation is exacerbated for helium which requires rather diffuse orbitals to obtain a converged band gap.

This situation is illustrated in Fig. 8, where we show the convergence of the band gap as a function of the basis set used for snapshots obtained using the trajectories calculated at $\rho=1$ g cm⁻³ and two different ion temperatures T_i . Figure 8 shows band gaps based on a single configuration randomly selected from the trajectory of interest. We further note that the hybrid calculations are performed at zero temperature. The temperature dependence results from the use of ionic configurations obtained from a trajectory corresponding to the thermodynamics conditions indicated. We show in Fig. 8 the GGA HOMO-LUMO band gap calculated at electronic temperatures $T_e=0$ and $T_e=T_i$ using a plane wave basis set in addition to a $T_e=0$ calculation with a Gaussian basis. The PW91 functional is used for the plane wave calculations, while the PBE and the hybrid PBE0 functionals are used for the calculations using a Gaussian basis set. We note that these two functionals are similar and should lead to very close results. We use the even tempered basis set proposed

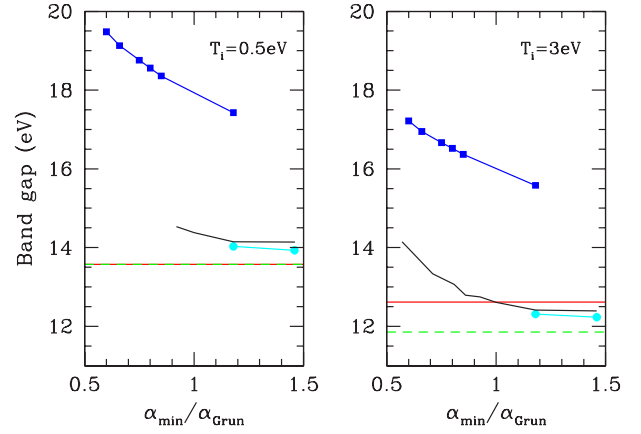


FIG. 8. (Color online) Convergence of the hybrid band gap as a function of Gaussian basis set for ionic temperature $T_i=0.5$ eV (left hand panel) and 3 eV (right hand panel) and a density of 1 g cm⁻³. Plane wave GGA (PW-PW91) band gaps with $T_e=T_i$ are shown by the horizontal lines (solid, red) and also for $T_e=0$ (dashed, green). The corresponding $T_e=0$ GGA (PBE0) band gap using a Gaussian basis set ($8s2p$)[$6s2p$] is shown by the solid curve (black). Adding a d orbital to the Gaussian basis set improves the agreement with the plane wave GGA calculation (filled circles, cyan). Finally, the hybrid functional band gap ($T_e=0$) with a Gaussian basis set ($8s2p$)[$6s2p$] is shown by the filled squares (blue). The band gaps shown are based on a single ionic configuration for each T_i .

by Grüneich and Hess⁶² ($10s2p$)[$6s2p$] and truncate the most diffuse s orbitals as the density is increased. The basis proposed for helium is reproduced in Table II for convenience. At a density of 1 g cm⁻³, we truncated the initial basis set to a ($8s2p$)/[$6s2p$] basis. Figure 8 shows the convergence of the band gap as the smallest Gaussian exponent α_{\min} is increased. The reference value, α_{Grun} , is the value of the smallest Gaussian exponent of the truncated basis at hand ($\alpha_{\text{Grun}}=0.126636a_0^{-2}$ at 1 g cm⁻³).

For both values of T_i , we see that the HOMO-LUMO band gap obtained using the PBE functional at $T_e=0$ is converged for $\alpha_{\min}/\alpha_{\text{Grun}} \geq 1.2$ and agrees to within 0.5 eV of the $T_e=0$ plane wave band gap. The difference can be further

TABLE II. Gaussian basis set used in the hybrid calculation.

| l | α_i (a_0^{-2}) | c_i |
|-----|---------------------------|--------------|
| s | 799.861 | 0.000709799 |
| | 113.852 | 0.0057978534 |
| | 25.5122 | 0.029432073 |
| | 7.27573 | 0.10662688 |
| | 2.40109 | 0.27193618 |
| s | 0.859007 | 1.0 |
| s | 0.324421 | 1.0 |
| s | 0.126636 | 1.0 |
| s | 0.0334228 | 1.0 |
| s | 0.0111537 | 1.0 |
| p | 1.73 | 1.0 |
| p | 0.58 | 1.0 |

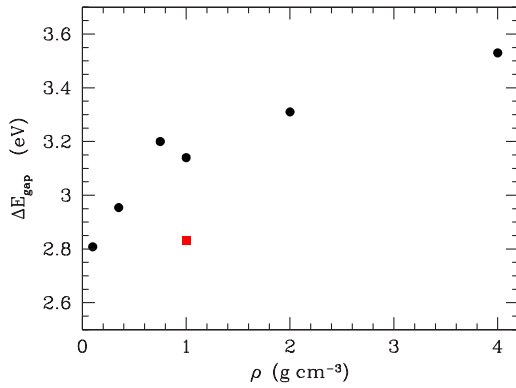


FIG. 9. (Color online) Correction to the GGA band gap from the hybrid functional DFT calculation. Filled circles show the density variation at $T_i=0.52$ eV. The filled square shows a point calculated at $T_i=3$ eV.

reduced down to ≤ 0.3 eV by adding a d orbital, as shown in Fig. 8. However, as our conductivity calculation is not sensitive to band gap variations of ≤ 0.5 eV, we retained the smaller basis to perform the more expensive PBE0 calculations that follow. We find that the additional correction obtained using the PBE0 functional is constant when α_{\min} is varied. We thus consider the PBE0 result converged for this same basis set by analogy with the PBE results. We finally note that the GGA (plane waves) band gap obtained at a temperature of $T_e=T_i=3$ eV is larger than the corresponding $T_e=0$ eV result (right panel). This result is consistent with LDA band gap calculations that show a universal increase with electronic temperature. On the other hand, GW calculations at finite electronic temperatures show a decreasing gap.⁵⁷ In all our calculations (GGA, GW, and hybrid), we find that the band gap decreases with increasing ionic temperature, a stronger effect than that caused by finite T_e .

Figure 9 shows the difference between the hybrid PBE0 and the GGA PW91 band gaps obtained using calculations that were performed on a single configuration randomly selected from the trajectory of interest. As before, the PBE0 calculations are performed at electronic temperature $T_e=0$. The band gap correction is ~ 3 eV and increases by about 0.7 eV as the density increases from 0.1 to 4 g/cm³. Using a configuration obtained at a temperature $T_i=3$ eV leads to a similar band gap correction of ~ 3 eV. While these variations could be physical, they remain well within the uncertainties of the calculation as the error bars on the GGA band gap alone are typically greater than 1 eV (Fig. 7).

C. GW calculation

A powerful method for the correction of the band gap is the GW approximation⁵² which we calculate with the ABINIT code.^{28,29} For this purpose, we generated ionic configurations with classical Monte Carlo (MC) simulations of 32 helium atoms interacting with an effective He-He pair potential.¹⁹ We have verified that these configurations give the same ion-ion pair correlation function and the same thermodynamics as full QMD simulations. This agreement reflects the fact that the He-He effective pair potential gives a very good

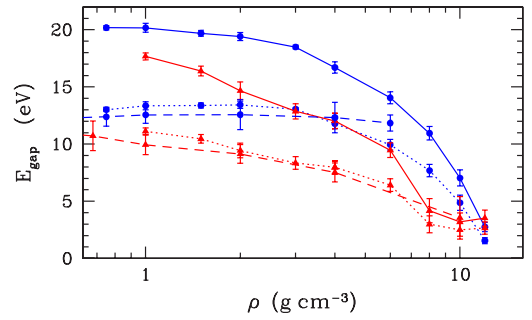


FIG. 10. (Color online) GGA and GW-corrected band gaps for $T_i=0.5$ eV (upper curves, blue) and 1.5 eV (lower curves, red). The ABINIT GGA calculations are shown by the dotted curves, and the GW-corrected band gap by the solid curves. Each point is the average of corrections computed for nine different ionic configurations obtained from classical MC simulations (see text). The dashed lines show the GGA band gap from Fig. 7.

description of He up to densities of ~ 2 g/cm³. The use of the classical MC configurations as the input for the ABINIT code is validated by the good agreement (better than 1 eV) we obtain for the GGA band gap with that from full QMD simulations we conducted using VASP with a larger number of particles (Fig. 10).

The GW calculation follows the standard implementation in ABINIT with the PBE functional (GGA) and are performed at $T_e=0$. The number of bands (250) and the plane wave cutoff (544 eV) were adjusted to ensure convergence of the GW band gap correction to within 0.1 eV. The GW band gap corrections at $T_i=0.5$ and 1.5 eV are shown on Fig. 10. At low densities, the GW correction is $\sim 6-7$ eV, and the band gap approaches the correct value for an isolated He atom, 19.82 eV. For $\rho \leq 6$ g cm⁻³, the band gap with the GW correction is $\sim 50\%$ larger than the KS band gap, which is consistent with the results of similar GGA and GW calculations for semiconductors.⁵²

We also note that while the hybrid functional and the GW calculations disagree on the value of the band gap correction by ~ 3 eV, they both show that it is independent of the density for $\rho \leq 4$ g cm⁻³. Our GW calculations are performed at zero electronic temperature. While this allows the recovery of the zero density band gap at low ionic temperature, and as such can be seen as the most accurate calculation, it is really an upper bound for the GW band gap at finite electronic temperature. The recent work of Faleev *et al.*⁵⁷ shows that the GW band gap of several materials decreases by up to ~ 1 eV for $T_e < 1.5$ eV. A finite temperature GW calculation should be performed to accurately establish the temperature dependence of the band gap correction for helium. Below, we apply corrections of +3 and +6 eV to the GGA band gap (for $\rho \leq 4$ g cm⁻³) as a representative illustration of the effect on the conductivity and reflectivity at high temperature and where experimental data are available.

VI. ELECTRICAL PROPERTIES

Figure 11 shows the variation of the dc conductivity along the 2000, 6000, and 17 406 K (1.5 eV) isotherms and for one

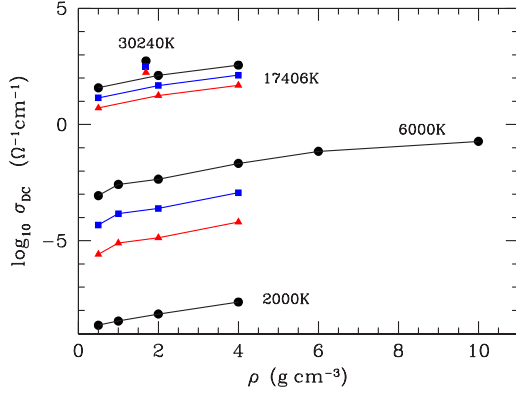


FIG. 11. (Color online) dc conductivity of helium based on MD-DFT simulations with the GGA functional (filled circles) and after applying band gap corrections of 3 eV (squares) and 6 eV (triangles). At densities above 4 g cm^{-3} , both the hybrid and GW band gap corrections are no longer constant and the corresponding conductivities are not shown.

value of the density at $T=30\,240 \text{ K}$. The dc conductivity is obtained by taking the zero frequency limit of Eq. (20). For all the conditions studied here, the optical conductivity has a Drude-like form for photon energies below 10 eV. This confirms that the opacity is dominated by the free-free contribution which, in turn, is directly related to the electrical conductivity and the ionization fraction. For the three isotherms shown in Fig. 11, we find that pressure ionization remains moderate (weak) at these densities. While the dc conductivity varies by about 2 orders of magnitude as the density is increased from 0.5 to 6 g cm^{-3} , the fluid remains essentially an insulator along the two lowest isotherms and up to the highest densities investigated. The temperature dependence of the dc conductivity is, in contrast, more drastic with an increase of over 10 orders of magnitude as the temperature is raised from 2000 to 17 406 K. Over the limited range where they overlap, the conductivities we calculate with the GGA functional are in very good agreement with those of Ref. 12. To estimate the uncertainties on the electrical properties resulting from the use of the ground state GGA method, we apply, as explained above, uniform $\Delta E = +3$ and $+6 \text{ eV}$ corrections to the GGA eigenenergies above the Fermi energy (E_m^k) when calculating the conductivities using Eq. (20). The occupation number f_n^k appearing in Eq. (20) also includes this correction to E_m^k . To first order, the matrix elements appearing in Eq. (20) do not need to be corrected.⁶³ In the limit where $kT \ll E_{\text{gap}}$, these approximations imply that the conductivity is reduced by a factor of $\exp(-\Delta E/2kT)$. Figure 11 also shows that the dc conductivity is significantly reduced when these band gap corrections are introduced and is very sensitive to the value of E_{gap} for $T \lesssim 1 \text{ eV}$. At the low temperature of 2000 K, the calculated conductivity reaches the limit of accuracy of the method and is given as an order of magnitude estimate only. For this reason, we do not apply any band gap correction at this particular temperature.

We also calculate the electrical conductivity from the ionization equilibrium of the He fluid obtained with the chemical model with a simple Drude approximation,

$$\sigma_{\text{dc}} = n(e)e^2/m_e \nu_{\text{eff}}, \quad (21)$$

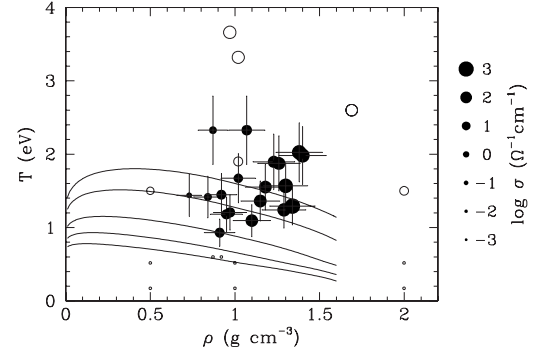


FIG. 12. Conductivity of helium as a function of ρ and T . The value of the conductivity is given by the size of the symbols, as shown by the scale at the right. The smallest symbols correspond to $\log_{10} \sigma_{\text{dc}} \leq -3$. Experimental values (Ref. 6) are shown by the solid circles with error bars. MD-DFT calculations of the conductivity after applying a $+6 \text{ eV}$ correction to the GGA band gap are shown by open circles. Contours show the conductivity from the chemical model for $\log_{10} \sigma_{\text{dc}} (\Omega^{-1} \text{ cm}^{-1}) = -3, -2, -1, 0, \text{ and } 0.5$, from bottom to top, respectively.

which is justified by the *ab initio* conductivities (see Sec. VII). The effective collision frequency ν_{eff} , corrected for density effects, is estimated with^{37,64}

$$\nu_{\text{eff}} = \nu_{\text{class}} [1 + 2\lambda_{\text{th}} \sigma_{\text{id}} n(\text{He})], \quad (22)$$

where

$$\nu_{\text{class}} = \sqrt{\frac{3kT}{m_e}} \sigma_{\text{id}} S(0) n(\text{He}), \quad (23)$$

λ_{th} is the thermal de Broglie wavelength of the electrons, $\sigma_{\text{id}} \sim 6 \text{ \AA}^2$ is the e -He scattering cross section for the dilute gas,⁴⁰ and $S(0)$ is the He-He structure factor that accounts for correlations.^{2,64}

The term $(1 + 2\lambda_{\text{th}} \sigma n)$ accounts for multiple scattering in a dense medium and is validated by experiments.^{37,64} Equation (21) is of marginal validity at the highest densities of interest here, however. The multiple scattering correction and the $S(0)$ correction become quite large for $\rho \geq 1 \text{ g cm}^{-3}$, each affecting σ_{dc} by an order of magnitude, but in opposite directions. Other expressions for ν_{eff} in dense fluids are of a heuristic nature and cannot be validated due to the lack of experimental data at such high densities.

Our calculations of the dc conductivity of helium with the MD-DFT (with a constant $+6 \text{ eV}$ correction to the GGA band gap) and with the chemical model are summarized in Fig. 12, where we also show experimental measurements of the conductivity under shock compression.^{6,65} The measurements clearly show that helium becomes a conductor akin to a poor metal ($\sigma_{\text{dc}} \sim 10^3 \Omega^{-1} \text{ cm}^{-1}$) at densities slightly above 1 g cm^{-3} . The measured conductivity rises rapidly with density and has only a very weak dependence on temperature. This behavior was attributed to pressure ionization⁶ or, equivalently, to the closing of the band gap.

Due to practical limitations, the experiments and the MD-DFT simulations sample only a few points on the $\sigma_{\text{dc}}(\rho, T)$ surface of helium (Fig. 12). The conductivity surface defined

by the MD-DFT points intersects that defined by the data and is within the same order of magnitude over a small region ($\rho \sim 0.9\text{--}1.2 \text{ g cm}^{-3}$ and $T \sim 1.3\text{--}2 \text{ eV}$). However, there is a striking difference in their *variation* with ρ and T , where the simulations show a weak density dependence and a rapid increase with temperature, which is the opposite of the trend seen in the data. In other words, the conductivity surfaces cross each other in a region probed by the experiment but their gradients are nearly orthogonal. The behavior of the *ab initio* conductivity follows from our band gap calculations, where under the experimental (ρ, T) conditions the gap remains wide ($>15 \text{ eV}$ compared to $kT \lesssim 2.4 \text{ eV}$ for the experiments) and essentially density independent for $\rho \sim 1\text{--}2 \text{ g cm}^{-3}$ (Figs. 7 and 10). Since $E_{\text{gap}} \gg kT$, there is a roughly exponential thermal excitation of electrons into the conduction band (Fig. 11). This behavior of the *ab initio* conductivities is firmly established by three different band gap calculations; using a GGA functional, using a hybrid functional, and computing a GW correction. All three show that the band gap is almost constant in density in the range shown in Fig. 12. The only difference between the three calculations is that they progressively increase the band gap, which reduces the conductivity by a factor that is weakly dependent on density (Fig. 11).

Where the region of validity of our chemical model overlaps the data, there is a rather poor agreement, with the chemical model predicting conductivities 1–2 orders of magnitude smaller. Generally, the chemical model and the QMD simulations give conductivities within the same order of magnitude at the low T where the former is applicable. Again, we find that the (ρ, T) dependence of the modeled conductivity is at odds with the data. In fact, contours of constant σ_{dc} drawn through the data in Fig. 12 are essentially perpendicular to the contours based on the chemical model. In this aspect, the latter is also in qualitative agreement with the QMD simulations.

Recent calculations of the dc conductivity of helium¹² using VASP (GGA functional) and with a chemical model are in generally good agreement with our results. As far as can be assessed from the published results, both *ab initio* calculations with a GGA functional give essentially identical conductivities. The chemical model^{66,67} gives conductivities generally three to ten times larger than ours, with a (ρ, T) dependence that agrees well with ours. Both chemical models show that the pressure ionization of helium occurs at $\rho > 1.6 \text{ g cm}^{-3}$. Nevertheless, Ref. 12 claims very good agreement with the experimental data. This apparent disagreement with the conclusion presented here arises from comparing the experimental conductivities with the calculations without considering the T dependence of the data. Figure 3 of Ref. 12 does not show that there is no trend in temperature along the steady rise of the experimental conductivity with density. For example, the highest conductivity measured ($1085 \Omega^{-1} \text{ cm}^{-1}$) corresponds to one of the lowest temperatures (15 000 K), while the calculations shown in Fig. 3 would imply that $T \geq 30\,000 \text{ K}$, above the upper limit of the temperatures achieved in the experiments. While conductivities typical of a metal are achieved in both the calculations and the experiments, they do so for different reasons. In the

models, it is very clearly a consequence of high temperature ($T \geq 2.5 \text{ eV}$), while in the data, it results from an increase in density ($\rho \geq 1.3 \text{ g cm}^{-3}$).

VII. OPTICAL PROPERTIES

We show in Figs. 13 and 14 the variation of the absorption coefficient $\alpha(\nu)$ and of the index of refraction $n(\nu)$ as a function of frequency ν for two temperatures. In agreement with the low value of the dc conductivity under these conditions, we find that the index of refraction and absorption coefficient are characteristic of an insulating atomic system. For helium, the first excitation energy is 19.82 eV. Accordingly, we find that the index of refraction drops below unity for photon energies $\geq 20 \text{ eV}$ at low density, while the absorption coefficient presents a maximum. This peak in absorption corresponds to bound-bound and bound-free transitions in the dilute gas. As the density increases along both isotherms, the index of refraction at photon energies below 10 eV increases from a value of about 1 to almost 2 at the highest density and temperature investigated. The increase in conductivity noted in Fig. 11 corresponds to an increase of the absorption coefficient at photon energies below 10 eV. In this photon energy range, the free-free absorption dominates the opacity. The variation of the absorption coefficient directly follows the variation of the dc conductivity and its frequency dependence is very similar to that of the Drude model of conductivity.

We compare in Fig. 15 the QMD index of refraction with a semiempirical virial expansion^{68–71}

$$n(\nu) = 1 + a(\nu)n(\text{He}) + b(\nu, T)n^2(\text{He}), \quad (24)$$

where

$$a(\nu) = 1.5913 \times 10^9 \left(\frac{0.6097}{\nu_a^2 - \nu^2} + \frac{1.065}{\nu_b^2 - \nu^2} \right) \text{ cm}^3, \quad (25)$$

$$b(\nu, T) = \frac{3}{2N_A^2} \left[-0.021\,92X^2 + 0.003\,96X + 0.084\,53 + \left(\frac{\nu}{\nu_0} \right)^2 (-0.010\,29X^2 - 0.311\,67X + 0.647\,37) \right] + \frac{a^2(\nu)}{6} \text{ cm}^6, \quad (26)$$

$X = \log_{10} T$ (K), $\nu_a = 5.413 \times 10^{15} \text{ Hz}$, $\nu_b = 9.771 \times 10^{16} \text{ Hz}$, $\nu_0 = 4.134\,14 \times 10^{16} \text{ Hz}$, and N_A is Avogadro's number. The expansion is valid as long as $n(\text{He}) < |a(\nu)/2b(\nu, T)|$. At both temperatures shown, the two calculations agree in the density dependence of the index of refraction. The largest difference between the two calculations appears at 2 g/cm^3 and $T = 2000 \text{ K}$ where the *ab initio* index of refraction is underestimated by a few percents.

We also compare the QMD-DFT absorption coefficients calculated at two different temperatures and densities with typical He^- free-free opacity calculation used in modeling the atmospheres of cool white dwarf stars.^{2,72,73} The latter uses the dilute gas He^- free-free cross section based on stan-

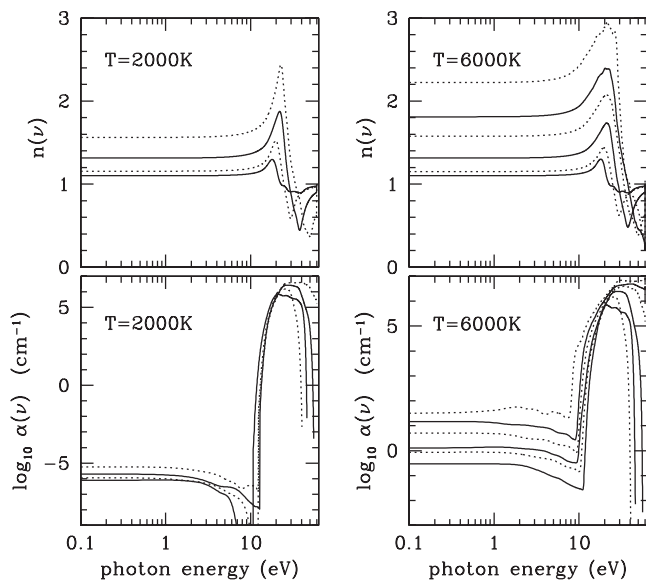


FIG. 13. The index of refraction $n(\nu)$ and the absorption coefficient $\alpha(\nu)$ as a function of photon energy. The left hand panels show the values for $T=2000\text{K}$ and densities of (from bottom to top) 0.5, 1, 2, and 4 g cm^{-3} . The right hand panels show the values for $T=6000\text{K}$ and densities of 0.5, 1, 2, 4, 8, and 10 g cm^{-3} . Note the change of scale for $\alpha(\nu)$. The low-energy, flat portion of the absorption coefficient corresponds to free-free transitions and the peak at $h\nu \gtrsim 20\text{ eV}$ corresponds to bound-bound and bound-free transitions in He.

standard electron scattering calculations.⁷⁴ The free electron density that enters the He^- free-free opacity is obtained from a chemical EOS for helium, which differs from the one presented here in that it only includes interactions between He atoms.⁷² Figure 15 shows two significant differences between the two calculations. First, the absorption coefficients differ by several orders of magnitude between the two calculations. This is a direct consequence of the huge difference between the number density of free electrons in this particular chemical model⁷² and the number density of electrons in the conduction band of the QMD-DFT calculation. These

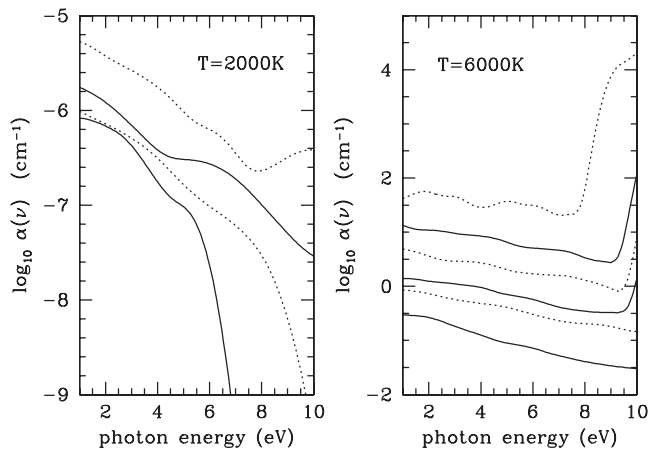


FIG. 14. Absorption coefficient for low-energy photons ($h\nu < 10\text{ eV}$). See Fig. 13 for details. The oscillations in some of the curves are not physical.

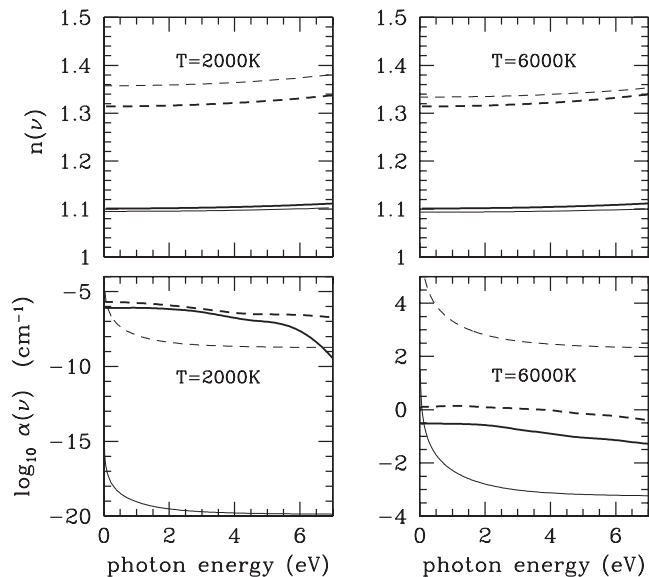


FIG. 15. Comparison between the index of refraction and the absorption coefficient obtained with QMD-DFT with other calculations for two temperatures and $\rho=0.5$ (solid curves) and 2 g cm^{-3} (dashed curves). The QMD calculations are shown with thick lines. The QMD-DFT index of refraction is compared with a semiempirical virial expansion [thin lines, Eq. (24)]. The absorption coefficient is compared to the He^- free-free absorption commonly used in modeling white dwarf atmospheres of pure helium composition (thin lines).

two quantities are equivalent concepts within their respective models. Second, the frequency dependence of the absorption coefficient is noticeably different, with the QMD-DFT calculation showing a nearly flat, Drude-like behavior and the dilute gas He^- free-free cross section diverging rapidly at low frequencies. The latter behavior is clearly unphysical since $\alpha(0)$ is proportional to σ_{dc} which is always finite.

At $T=2000\text{K}$, the standard He^- free-free opacity is 2–13 orders of magnitude lower than that of the QMD-DFT simulations for $0.5 \leq \rho \leq 2\text{ g cm}^{-3}$. At higher temperature ($T=6000\text{K}$), the discrepancy is smaller, about 2 orders of magnitude, with the standard calculation ultimately becoming larger than the QMD-DFT results. This indicates that the pressure ionization is too abrupt in the model of Ref. 72.

On the other hand, a rather good agreement between the two EOSs was found in that regime. This comparison indicates that in this regime of very low ionization fraction where the free electron density does not contribute significantly to the total pressure and energy, current chemical models for helium can reliably provide the thermodynamics but are inadequate for the calculation of the abundances of the charged species that largely determine the opacity of the fluid.

In addition to the conductivity, reflectivity is another potential experimental probe of the state of helium at high densities. The increase of reflectivity with temperature at a density of $\sim 1\text{ g cm}^{-3}$ is shown in Fig. 16. These conditions correspond to the regime where measurements are currently under way. The reflectivity remains very small for $T \lesssim 2\text{ eV}$ but rises rapidly to measurable values at higher temperatures.

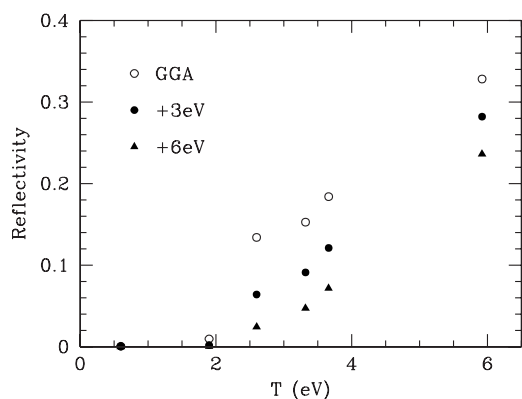


FIG. 16. Temperature dependence of the reflectivity of pure helium at densities near 1 g cm^{-3} and a wavelength of 542 nm . The points at $T=1.9 \text{ eV}$ are computed for a slightly higher density of 1.69 g cm^{-3} . These correspond to a subset of the MD-DFT conductivities shown in Fig. 11. For each value of the temperature, the reflectivity is computed with the MD-DFT with (1) the GGA band gap (open circles), (2) the GGA band gap with a +3 eV correction (filled circles), and (3) the GGA band gap with a +6 eV correction (filled triangles).

The increase shown in Fig. 16 is only a temperature effect and is due to the reduction of the band gap shown in Fig. 7 and an increase in the occupation of the conduction band. The sensitivity to the band gap correction is significant and reflectivity measurements should allow a measure of $E_{\text{gap}}(\rho, T)$ for helium in the regime of warm dense matter.

The dramatic differences in the opacity of helium shown in Fig. 15 will have a large effect on atmosphere models of helium white dwarfs.⁷⁵ The flatter Drude-like opacity of the DFT simulations will affect the near-infrared flux in model spectra. With the higher He^- free-free opacity, the contribution of Rayleigh scattering (not shown in Fig. 15) becomes nearly negligible. The resulting opacity is nearly frequency independent, with a noticeable effect on the modeled spectrum. More significantly, the overall increase in opacity will lengthen the cooling time scale of cool white dwarfs with pure helium atmospheres. In some (and perhaps all) cool helium-rich atmospheres of white dwarfs, traces of hydrogen and of heavier elements are inferred or observed. These elements ionize more readily than helium and, if sufficiently abundant, can dramatically increase the opacity either by increasing the He^- free-free opacity or perhaps by forming H^- . Such “pollution” of the atmosphere may have a larger effect than the increased opacity that we report here for pure He. However, a better understanding of the limiting case of pure helium atmospheres is an important aspect of unraveling the properties of the coolest white dwarfs known. For example, the atmospheric composition of very cool white dwarfs is determined solely from fits of the observed spectral energy distribution with models and, if present, of absorption lines from heavier elements. The use of synthetic spectra based on our modeled helium opacities will lead to revisions in the inferred compositions.⁷⁶

VIII. CONCLUSION

Using quantum molecular dynamics, we calculate the dynamical and electrical properties of helium in a regime rel-

evant to white dwarf atmospheres and compare them to EOS and conductivity measurements. We find very good agreement with the experimental principal and second-shock Hugoniot below 1 g/cm^3 . As the experimental measurements at high pressures are sparse, the current study provides a useful benchmark for EOS modeling above 1 g/cm^3 .

For the purpose of computing the optical properties of warm dense helium, we have done an extensive study of the band gap of helium with the density functional theory with a GGA functional (PW91). We have calculated zero temperature corrections to the band gap with a hybrid functional (PBE0) and the GW method. We find that the GGA band gap decreases slowly with increasing density and closes around $12\text{--}14 \text{ g cm}^{-3}$. We find that the gap decreases rapidly as the temperature increases beyond 1.5 eV . The band gap is about 15 eV at low temperature and density, which is about 5 eV below the value for the isolated atom. The GW correction adds $\sim 6 \text{ eV}$ to the GGA band gap and essentially recovers the isolated atom value at low density. The hybrid functional calculation increases the GGA band gap by $\sim 3 \text{ eV}$. Both the GW and hybrid calculations are performed at zero electronic temperature and, as such, are upper bounds to the band gap correction. We have computed conductivities within the linear response theory from the results of the GGA calculation and with +3 and +6 eV corrections to illustrate the effects anticipated from more accurate band gap calculations at finite electronic temperature.

We have developed a chemical model of low-temperature, low-density helium where the ionization fraction remains small ($\leq 0.1\%$). This model includes interactions between all species and atomic He. The $e\text{-He}$ interaction, in particular, was modeled with DFT calculations rather than assuming some pair interaction potential. By construction of the He-He effective potential, this model also reproduces the first- and second-shock Hugoniot data. The conductivity can be calculated from the density of free electrons predicted by this model.

The experimental conductivities cannot be reconciled either with the *ab initio* QMD or with the chemical model. A few experimental (ρ, T) points agree well with the QMD-DFT conductivities but there is a striking disagreement in their density and temperature dependence. The surfaces $\sigma_{\text{dc}}(\rho, T)$ defined by the data and the QMD-DFT simulations intersect in the region covered by the data (roughly 1 g cm^{-3} and $1\text{--}2 \text{ eV}$), but their large gradients are nearly orthogonal to each other. Our calculations show a strong dependence on temperature because the band gap in the QMD simulations remains much larger than kT in the regime of interest. The range of validity of the chemical model is limited to low temperatures and moderate densities, compared to the data, and the agreement is poor. Nonetheless, the trends with temperature and density generally follow those of the QMD-DFT calculations.

Disagreements between the data and the chemical model may be expected as it is difficult to estimate the importance of N -body effects on the He-He^+ interaction potential (which determines in large part the ionization fraction in the model) and that the expression for $e\text{-He}$ collision frequency in the estimation of the Drude dc conductivity is of limited validity when multiple scattering and correlations become important.

The differences between the data, the chemical model, and the QMD simulations arise principally from the different implied values for the density where pressure ionization occurs in helium. The experimental results can be understood only if the pressure ionization (alternatively, the closing of the band gap) occurs at $\rho \sim 1.4 \text{ g/cm}^3$. The QMD simulations show that the band gap is 15–20 eV at this density (depending on temperature). It would be rather surprising if helium, with its tightly bound, closed-shell electronic structure would pressure ionize at approximately the same density as hydrogen, as the data suggest. While the calculations performed here provide a solid benchmark for physical models to describe He at conditions found in white dwarf atmospheres, the significant disagreement with the currently

available conductivity data calls for additional measurements to firmly establish the density where helium becomes pressure ionized. Ongoing reflectivity measurements under shock compression may prove useful in resolving this discrepancy.

ACKNOWLEDGMENTS

We thank P. Celliers and P. Loubeyre for useful discussions and sharing experimental results prior to publication. We also thank V. E. Fortov for sharing unpublished experimental data. This work was supported under the auspices of the U.S. Department of Energy at Los Alamos National Laboratory under Contract No. W-7405-ENG-36.

-
- ¹G. Fontaine, P. Brassard, and P. Bergeron, *Publ. Astron. Soc. Pac.* **113**, 409 (2001).
- ²C. A. Iglesias, F. J. Rogers, and D. Saumon, *Astrophys. J.* **569**, L111 (2002).
- ³D. Saumon and T. Guillot, *Astrophys. J.* **609**, 1170 (2004).
- ⁴T. Guillot, *Science* **286**, 72 (1999).
- ⁵W. J. Nellis, N. C. Holmes, A. C. Mitchell, R. J. Trainor, G. K. Governio, M. Ross, and D. A. Young, *Phys. Rev. Lett.* **53**, 1248 (1984).
- ⁶V. E. Fortov, V. Ya. Ternovoĭ, M. V. Zhernokletov, M. A. Mochalov, A. L. Milkhalov, A. S. Filimonov, A. A. Pyalling, V. B. Mintsev, V. K. Gryaznov, and I. L. Iosilevskii, *JETP* **97**, 259 (2003).
- ⁷P. M. Cellier and P. Loubeyre (private communication); S. Brygoo, PhD thesis. Ecole Polytechnique, France (2006).
- ⁸G. Fontaine, H. C. Graboske, and H. M. Van Horn, *Astrophys. J., Suppl.* **35**, 293 (1977).
- ⁹D. Saumon, G. Chabrier, and H. M. Van Horn, *Astrophys. J., Suppl. Ser.* **99**, 713 (1995).
- ¹⁰C. Winisdoerffer and G. Chabrier, *Phys. Rev. E* **71**, 026402 (2005).
- ¹¹B. Militzer, *Phys. Rev. Lett.* **97**, 175501 (2006).
- ¹²A. Kietzmann, B. Holst, R. Redmer, M. P. Desjarlais, and T. R. Mattsson, *Phys. Rev. Lett.* **98**, 190602 (2007).
- ¹³N. D. Mermin, *Phys. Rev.* **137**, A1441 (1965).
- ¹⁴J. Callaway, *Quantum Theory of the Solid State* (Academic, New York, 1974).
- ¹⁵W. A. Harrison, *Solid State Theory* (McGraw-Hill, New York, 1970).
- ¹⁶R. M. Martin, *Electronic Structure* (Cambridge University Press, New York, 2004).
- ¹⁷P. C. Stancil, *Astrophys. J.* **430**, 360 (1994).
- ¹⁸K. P. Huber and G. Herzberg, *Molecular Spectra and Molecular Structure. IV. Constants of Diatomic Molecules* (Van Nostrand Reinhold, New York, 1979).
- ¹⁹M. Ross and D. A. Young, *Phys. Lett. A* **118**, 463 (1986).
- ²⁰E. Scifoni, G. Dellepiane, and F. A. Gianturco, *Eur. Phys. J. D* **30**, 353 (2004).
- ²¹R. P. Marchi and F. T. Smith, *Phys. Rev.* **139**, A1025 (1965).
- ²²R. E. Olson and C. R. Mueller, *J. Chem. Phys.* **46**, 3810 (1967).
- ²³W. D. Kraeft, D. Kremp, W. Ebeling, and G. Röpke, *Quantum Statistics of Charged Particle Systems* (Plenum, New York 1986).
- ²⁴W. Ebeling, A. Förster, W. Richert, and H. Hess, *Physica A* **150**, 159 (1988).
- ²⁵D. Saumon and G. Chabrier, *Phys. Rev. A* **46**, 2084 (1992).
- ²⁶N. R. Kestner, J. Jortner, M. H. Cohen, and S. A. Rice, *Phys. Rev.* **140**, A56 (1965).
- ²⁷M. P. Allen and D. Tildesley, *Computer Simulation of Liquids* (Clarendon, Oxford, 1987).
- ²⁸X. Gonze, J.-M. Beuken, R. Caracas, F. Detraux, M. Fuchs, G.-M. Rignanese, L. Sindic, M. Verstraete, G. Zerah, F. Jollet, M. Torrent, A. Roy, M. Mikami, Ph. Ghosez, J.-Y. Raty, and D. C. Allan, *Comput. Mater. Sci.* **25**, 478 (2002).
- ²⁹X. Gonze, G.-M. Rignanese, M. Verstraete, J.-M. Beuken, Y. Pouillon, R. Caracas, F. Jollet, M. Torrent, G. Zerah, M. Mikami, Ph. Ghosez, M. Veithen, J.-Y. Raty, V. Olevano, F. Bruneval, L. Reining, R. Godby, G. Onida, D. R. Hamann, and D. C. Allan, *Z. Kristallogr.* **220**, 558 (2005).
- ³⁰S. Goedecker, M. Teter, and J. Hutter, *Phys. Rev. B* **54**, 1703 (1996).
- ³¹J. P. Perdew, K. Burke, and M. Ernzerhof, *Phys. Rev. Lett.* **77**, 3865 (1996).
- ³²S. Baroni, A. Dal Corso, S. de Gironcoli, P. Giannozzi, C. Cavazzoni, G. Ballabio, S. Scandolo, G. Chiarotti, P. Focher, A. Pasquarello, K. Laasonen, A. Trave, R. Car, N. Marzari, and A. Kokalj, <http://www.pwscf.org/>
- ³³A. D. Becke, *J. Chem. Phys.* **98**, 5648 (1993).
- ³⁴C. Lee, W. Yang, and R. G. Parr, *Phys. Rev. B* **37**, 785 (1988).
- ³⁵G. S. Tschumper and H. F. Schaefer, *J. Chem. Phys.* **107**, 2529 (1997).
- ³⁶J. R. Broomall, W. D. Johnson, and D. G. Onn, *Phys. Rev. B* **14**, 2819 (1976).
- ³⁷K. W. Schwarz, *Phys. Rev. Lett.* **41**, 239 (1978).
- ³⁸L. L. Tankersley, *J. Low Temp. Phys.* **11**, 451 (1973).
- ³⁹T. F. O'Malley, P. G. Burke, and K. A. Berrington, *J. Phys. B* **12**, 953 (1979).
- ⁴⁰J. Yuan, *J. Phys. B* **21**, 3753 (1988).
- ⁴¹B. Boltjes, C. de Graaf, and S. W. de Leeuw, *J. Chem. Phys.* **98**, 592 (1993).
- ⁴²G. Kresse and J. Hafner, *Phys. Rev. B* **47**, RC558 (1993); G. Kresse and J. Furthmüller, *Comput. Mater. Sci.* **6**, 15 (1996);

- Phys. Rev. B **54**, 11169 (1996).
- ⁴³J. P. Perdew and Y. Wang, Phys. Rev. B **46**, 12947 (1992).
- ⁴⁴P. E. Blochl, Phys. Rev. B **50**, 17953 (1994); G. Kresse and D. Joubert, *ibid.* **59**, 1758 (1999).
- ⁴⁵M. P. Desjarlais, Phys. Rev. B **68**, 064204 (2003).
- ⁴⁶Ya. Zeldovich and Yu. Raizer, *Physics of Shock Waves and High-Temperature Hydrodynamic Phenomena* (Academic Press, New York, 1966).
- ⁴⁷J. D. Kress, S. Mazevet, L. A. Collins, and W. W. Wood, Phys. Rev. B **63**, 024203 (2001).
- ⁴⁸H. J. Monkhorst and J. D. Pack, Phys. Rev. B **13**, 5188 (1976).
- ⁴⁹S. Mazevet, J. Kress, and L. A. Collins, *Atomic Processes in Plasmas*, AIP Conf. Proc. No. 730 (AIP, Melville, 2004), p. 139.
- ⁵⁰D. A. Young, A. K. McMahan, and M. Ross, Phys. Rev. B **24**, 5119 (1981).
- ⁵¹1 eV = 11 605 K.
- ⁵²K. A. Johnson and N. W. Ashcroft, Phys. Rev. B **58**, 15548 (1998).
- ⁵³O. A. Vyrhov and G. E. Scuseria, J. Chem. Phys. **122**, 184107 (2005).
- ⁵⁴J. P. Perdew and M. Levy, Phys. Rev. B **56**, 16021 (1997).
- ⁵⁵R. W. Godby, M. Schluter, and L. J. Sham, Phys. Rev. Lett. **56**, 2415 (1986).
- ⁵⁶G. Onida, L. Reining, and A. Rubio, Rev. Mod. Phys. **74**, 601 (2002).
- ⁵⁷S. V. Faleev, M. van Schilfgaarde, T. Kotani, F. Léonard, and M. P. Desjarlais, Phys. Rev. B **74**, 033101 (2006).
- ⁵⁸C. Adamo and V. Barone, J. Chem. Phys. **110**, 6158 (1999).
- ⁵⁹M. Challacombe, C. J. Tymczak, K. Nemeth, V. Weber, C. K. Gan, E. Schwegler, G. Henkelman, and A. Niklasson, Los Alamos National Laboratory Report No. LA-CC-04-086, 2004 (unpublished).
- ⁶⁰J. P. Perdew, M. Ernzerhof, and K. Burke, J. Chem. Phys. **105**, 9982 (1996).
- ⁶¹W. G. Aulbur, M. Stadele, and A. Gorling, Phys. Rev. B **62**, 7121 (2000).
- ⁶²A. Grüneich and B. A. Hess, Theor. Chem. Acc. **100**, 253 (1998).
- ⁶³L. Hedin, Phys. Rev. **139**, A796 (1965).
- ⁶⁴V. E. Fortov and I. T. Iakubov, *The Physics of Non-Ideal Plasma* (World Scientific, Singapore, 2000).
- ⁶⁵V. E. Fortov (private communication).
- ⁶⁶R. Redmer, H. Juranek, S. Kuhlbrodt, and V. Schwarz, Z. Phys. Chem. **217**, 783 (2003).
- ⁶⁷S. Kuhlbrodt, R. Redmer, H. Reinholz, G. Röpke, B. Holst, V. B. Mintsev, V. K. Gryaznov, N. S. Shilkin, and V. E. Fortov, Contrib. Plasma Phys. **45**, 61 (2005).
- ⁶⁸P. W. Langhoff and M. Karplus, J. Opt. Soc. Am. **59**, 863 (1969).
- ⁶⁹H. Koch, C. Hättig, H. Larsen, J. Olsen, P. Jørgensen, B. Fernández, and A. Rizzo, J. Chem. Phys. **111**, 10108 (1999).
- ⁷⁰R. Moszynski, T. G. A. Heijmen, and A. van der Avoird, Chem. Phys. Lett. **247**, 440 (1995).
- ⁷¹C. Hättig, H. Larsen, J. Olsen, P. Jørgensen, H. Koch, B. Fernández, and A. Rizzo, J. Chem. Phys. **111**, 10099 (1999).
- ⁷²P. Bergeron, D. Saumon, and F. Wesemael, Astrophys. J. **443**, 764 (1995).
- ⁷³Rayleigh scattering by He atoms is another potentially important opacity source in helium white dwarf atmospheres. Since the Kubo-Greenwood formalism is a linear response theory, Rayleigh scattering is not included in the opacity from the QMD-DFT simulations and is not discussed further here.
- ⁷⁴K. L. Bell, K. A. Berrington, and J. P. Croskery, J. Phys. B **15**, 977 (1982).
- ⁷⁵P. M. Kowalski, D. Saumon, and S. Mazevet, ASP Conf. Ser. **334**, 203 (2005).
- ⁷⁶D. Saumon, P. M. Kowalski, and S. Mazevet, in 15th European Workshop on White Dwarfs, edited by M. Burleigh and R. Napiwotzki, (unpublished).